



Photocatalytic NO removal over defective Bi/BiOBr nanoflowers: The inhibition of toxic NO₂ intermediate via high humidity

Yue Xin^{a,b,1}, Qiuhui Zhu^{b,1}, Ting Gao^b, Ximing Li^b, Wei Zhang^b, Hui Wang^b, Donghang Ji^b, Yu Huang^{c,d}, Mohsen Padervand^{e,*}, Feng Yu^a, Chuanyi Wang^{a,b,**}

^a Key Laboratory for Green Processing of Chemical Engineering of Xinjiang Bingtuan, School of Chemistry and Chemical Engineering, Shihezi University, Shihezi 832003, PR China

^b School of Environmental Science and Engineering, Shaanxi University of Science and Technology, Xi'an 710021, PR China

^c Key Laboratory of Aerosol Chemistry and Physics, State Key Lab of Loess and Quaternary Geology (SKLLQG), Institute of Earth Environment, Chinese Academy of Sciences, Xi'an 710061, PR China

^d CAS Center for Excellence in Quaternary Science and Global Change, Institute of Earth Environment, Chinese Academy of Sciences, Xi'an 710061, PR China

^e Department of Chemistry, Faculty of Science, University of Maragheh, P.O. Box 55181-83111, Maragheh, Iran

ARTICLE INFO

Keywords:

Photocatalysis
Humidity
Bi/BiOBr nanoflowers
Oxygen vacancies
NO removal

ABSTRACT

Water vapor (relative humidity) is an ineluctable factor for photocatalytic removal of low-concentration NO in practical environment. In this work, defective Bi/BiOBr nanoflowers were synthesized by a solvothermal approach. Benefiting from bismuth and oxygen vacancies, the efficiency of photocatalytic NO removal increased from the initial 26 % to 63 % when exposed to visible light. Furthermore, photocatalytic NO removal performance at various relative humidity levels was explored. It was found that the NO removal efficiency was negligibly affected by humidity. However, the generation of toxic NO₂ intermediate was reduced progressively from 87 to 29 ppb as the humidity increased from 5 % to 100 %, which may be attributed to the high hydrophilicity of NO₂. The NO-TPD and in-situ DRIFTS were further employed to unveil the pathway of adsorption and photocatalytic removal of NO. This study discloses a strategy for effectively removing NO from the atmosphere by reducing emission of harmful intermediate NO₂.

1. Introduction

As a typical pollutant in the air, NO is emitted after the combustion of fossil energy, which can cause acid rain, photochemical smog and other environmental crises [1,2]. Therefore, developing effective strategies to alleviate the harm caused by NO_x is always a challenge for air purification [3]. Conventional NO removal technologies mainly include bio-filtration, physical adsorption and thermal catalysis [4]. However, when it comes to tackling low-concentration NO_x in the control of practical air pollutants, the aforementioned solutions are not economical and/or efficient [5].

Since Fujishima and Honda reported n-TiO₂ for photoelectrocatalytic water splitting into H₂ in 1972, semiconducting-based photocatalysis has been developed into a relatively complete and multi-disciplinary

research system [6,7]. The photogenerated electrons (e⁻) and holes (h⁺) in semiconductor materials with suitable bandgap energy can migrate to the surface and react with the adsorbed O₂ and H₂O molecules to produce reactive oxygen species (ROSSs) such as superoxide radicals (•O₂⁻), hydroxyl radicals (•OH) and others [8]. The ROSSs can oxidize pollutants with the aim of environmental remediation, which has been confirmed as an efficient and environmentally-friendly strategy for NO removal from the air [9]. BiOBr as one of the oxyhalides is composed of (Bi₂O₃)²⁺ and Br⁻, which is a promising photocatalyst because of its exceptional electronic, excellent visible light response and cost effectiveness [10]. Nevertheless, the photocatalytic performance of pristine BiOBr is insufficient for the practical applications due to high electron-hole recombination rate and weak light harvesting properties [11].

* Corresponding author.

** Corresponding author at: Key Laboratory for Green Processing of Chemical Engineering of Xinjiang Bingtuan, School of Chemistry and Chemical Engineering, Shihezi University, Shihezi 832003, PR China.

E-mail addresses: padervand@maragheh.ac.ir (M. Padervand), wangchuanyi@sust.edu.cn (C. Wang).

¹ These authors contribute equally.

Many studies have shown that metals-loaded semiconductors can increase the separation effectiveness of photogenerated carriers via the surface plasmonic resonance (SPR) effect and Schottky barrier [12,13]. Additionally, semimetal bismuth (Bi) has the potential to be an effective alternative for the noble metals [14]. Oxygen vacancies (OVs) are also revealed to be an important factor in adjusting the optical and photocatalytic properties [15]. On one hand, the generation of oxygen vacancies promotes surface O_2 adsorption, making it easier for the captured electrons to reduce the adsorbed O_2 molecules to $\bullet O_2^-$ [16]. OVs with their usual defect states, on the other hand, can trap e^- or h^+ to impede photogenerated carriers recombination and enhance the transfer of charge carriers to the surface reactants [17]. Therefore, the synergistic effect of metallic Bi and OVs is advantageous for improving the photocatalytic performance of visible-light photocatalysts [18]. H_2O is always present in practical photocatalytic applications whereas it may play the vital role in the photocatalytic NO removal. However, relative humidity is rarely explored in the study of photocatalytic NO conversion, and the role of H_2O molecules is often disregarded in the conversion of NO to nitrate by ROS. These concerns deserve to be further investigated, such as if there is a competitive adsorption behavior between H_2O and NO molecules, and whether water molecules participate in the oxidation of nitric oxide to nitrate by reactive oxygen species.

In this work, Bi/BiOBr nanoflowers with OVs were produced by a simple one-pot solvothermal chemical reduction procedure using water/ethanol as solvent. As the proportion of ethanol increased, the morphology of BiOBr evolved from its initial nanosheet to a nanoflower structure, with the generation of oxygen vacancies and metallic bismuth. At the same time, the Bi/BiOBr nanoflowers exhibited improved photocatalytic performance for NO conversion when exposed to visible light in a constant air flow. The enhanced photocatalytic performance and decreased NO_2 generation may be attributed to the synergistic interaction between metallic Bi and OVs, which optimized the process of photocatalytic carriers' dynamics to accelerate the generation of ROS and widened the light response region. In addition, the influence of relative humidity on the photocatalytic performance was comprehensively investigated, indicating that high humidity can promote the transformation of toxic intermediate NO_2 to NO_3^- . Finally, based on the results of temperature-programmed desorption of NO (NO-TPD) and in-situ diffuse reflectance infrared fourier transform spectroscopy (DRIFTS), the mechanism of NO adsorption and enhanced photocatalytic activity over BOB-25 was elucidated.

2. Experimental

2.1. Materials and preparation

Without further purification, all drugs and reagents were of analytical grade. Typically, 2 mmol $Bi(NO_3)_3 \cdot 5 H_2O$ and 2 mmol KBr were added to 25 mL solvent composed of ethanol and water in different volume ratios with stirring in a 50 mL beaker for 1 h at ambient temperature. The solution was then adjusted with NaOH to achieve a pH of 11.3 (except for that with water only as the solvent). The mixture was stirred for 1 h before being put into a stainless-steel autoclave with Teflon lining to undergo a 24-hour hydrothermal procedure at 180 °C. After natural cooling to ambient temperature, the solid precipitates were gathered and separated by centrifuging, completely washing with ultrapure water and anhydrous ethanol, and then dried at 60 °C for 8 h. The samples prepared with x mL (x = 0, 5, 10, 15, 20, and 25) ethanol were denoted as BOB, BOB-5, BOB-10, BOB-15, BOB-20 and BOB-25, respectively.

2.2. Characterizations

X-ray powder diffraction (XRD) with powerful Cu K α radiation (model D/max2200PC, Rigaku Co., Japan) was used to characterize phase identifications. Micromorphology was performed with a scanning

electron microscope (SEM, FEI Verios 460, USA) and transmission electron microscopy (TEM, JEM-2010, Japan). The Edinburgh FLSP 920 fluorescence spectrometer was used to measure the photoluminescence spectra and decay curves. The adsorption-desorption curves for nitrogen were obtained using a Micromeritics device (ASAP-2020, USA). Measurements of electron spin resonance (ESR) were performed with a Bruker E500 equipment. The ESR signals of ROS were spin-trapped by 5,5-dimethyl-1-pyrroline N-oxide (DMPO). The samples were dissolved in DMPO aqueous solution and DMPO methanol solution to detect superoxide radicals and hydroxyl radicals, respectively. The visible light illumination was provided by a 300 W Xenon lamp with a 420 nm UV cut-off filter. A UV-vis diffuse spectrophotometer (UV-3700, Shimadzu, Japan) was utilized to analyze the optical characteristics of the samples in the 200–800 nm range, with 100 % $BaSO_4$ serving as the reference material. The surface chemical compositions, electronic states and valence band measurements were taken on a X-ray photoelectron spectroscopy (XPS) apparatus equipped with Al K α X rays (AXIS Supra, Kratos, Japan). X-ray photoelectron spectroscopy (XPS) is a surface-sensitive quantitative spectroscopic technique. The formed Bi^0 on the surface of BOB-25 tends to be oxidized by oxygen in air, therefore, it is difficult to detect the as-attributed peaks by XPS in a conventional way. As a result, BOB-25 needs to be etched with argon ion for XPS detection. The etching parameters are as follows: 1.5 mm etching spot size, 3000 eV etching voltage and 10 nm etching depth. The C 1s peak (284.8 eV) served as a calibration standard for all binding energies.

2.3. The assessment of photocatalytic performance

The photocatalytic performance was examined by the removal rate of NO at ppb concentrations in a reactor with continuous flow at room temperature (Fig. S1). The glass reactor with quartz cover has a volume of 0.785 L (R = 5 cm, L = 10 cm). For each test, 0.05 g sample was ultrasonically dispersed in 20 mL of distilled water to form an emulsion before being moved to a glass dish with a 6 cm diameter. And the dish coated with samples was dried at 60 °C to eliminate water before the test. A 300 W commercial Xenon lamp (with a 420 nm cut-off filter) was placed above the reactor and the vertical distance between the sample and the xenon lamp was about 15 cm. The NO concentration at the start was regulated to approximately 800 ppb by an air flow with the relative humidity of 5 %. The air and NO flow rates were set to 289 mL·min⁻¹ and 12.9 mL·min⁻¹, respectively. The lamp was turned on after the gas adsorption balance was reached. The concentration of NO and NO_x (NO + NO₂) was measured and constantly recorded each minute using a 42c-TL (Thermo Fisher Scientific, USA) NO_x analyzer. The removal efficiency (η) was calculated as $\eta = (1 - C/C_0) \times 100 \%$, and the NO_2 yield was calculated as follows: $\eta_{NO_2} = C_{NO_2}/(C_0 - C) \times 100 \%$, where C_0 and C are the inlet and outlet NO concentrations after achievement of adsorption-desorption equilibrium, respectively, and C_{NO_2} indicates the real-time NO_2 concentration.

3. Results and discussion

3.1. Crystal structure and morphology

XRD was employed to identify the phase architecture and crystallinity of as-prepared photocatalysts. As depicted in Fig. 1a, the samples' diffraction peaks are well-concordant with those of tetragonal BiOBr (JCPDS No. 09-0393), where the diffraction peaks appearing at 25.2, 31.7, 32.2 and 57.1° correspond to the (101), (102), (110) and (212) planes, respectively. Apart from the diffraction peaks of BiOBr, the characteristic peaks of metallic Bi (JCPDS No. 44-1246) can be clearly detected with the addition of alcohol, showing that Bi/BiOBr composites were successfully prepared.

The fabrication of Bi/BiOBr composites by a simple solvothermal process is demonstrated in Scheme 1a. SEM was used to check out the morphology and microstructure of the photocatalysts. As shown in

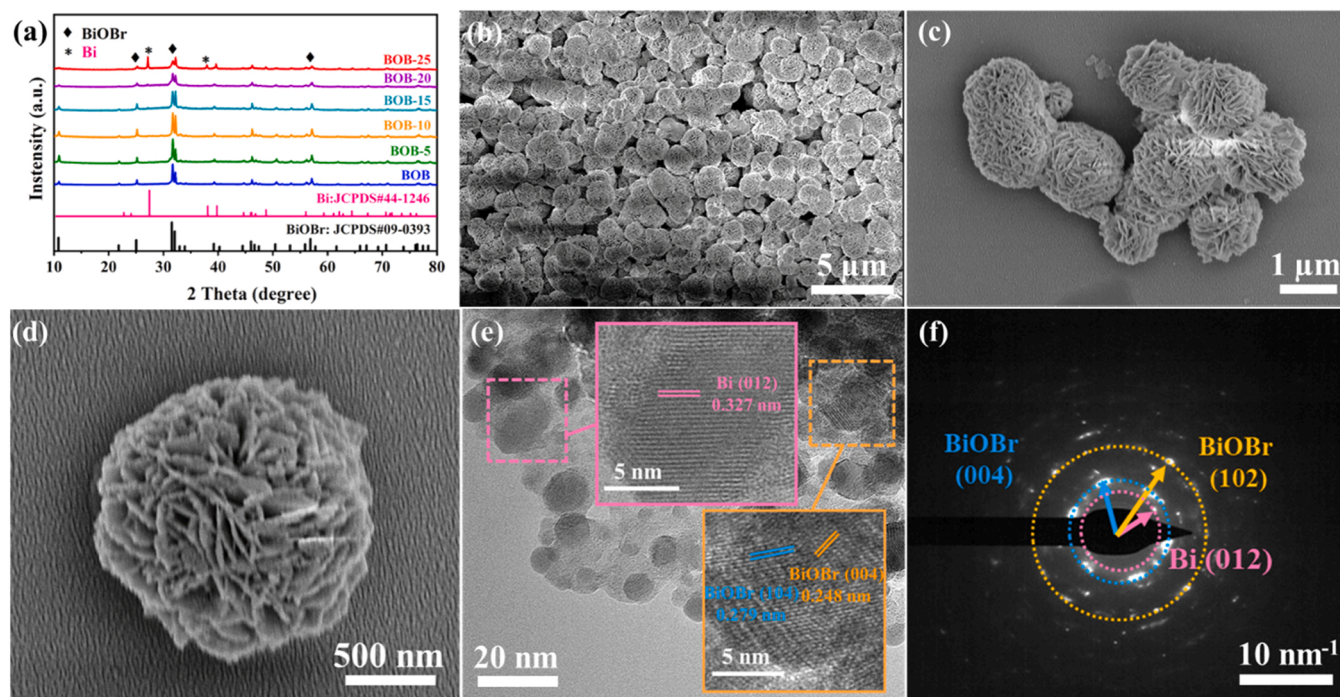
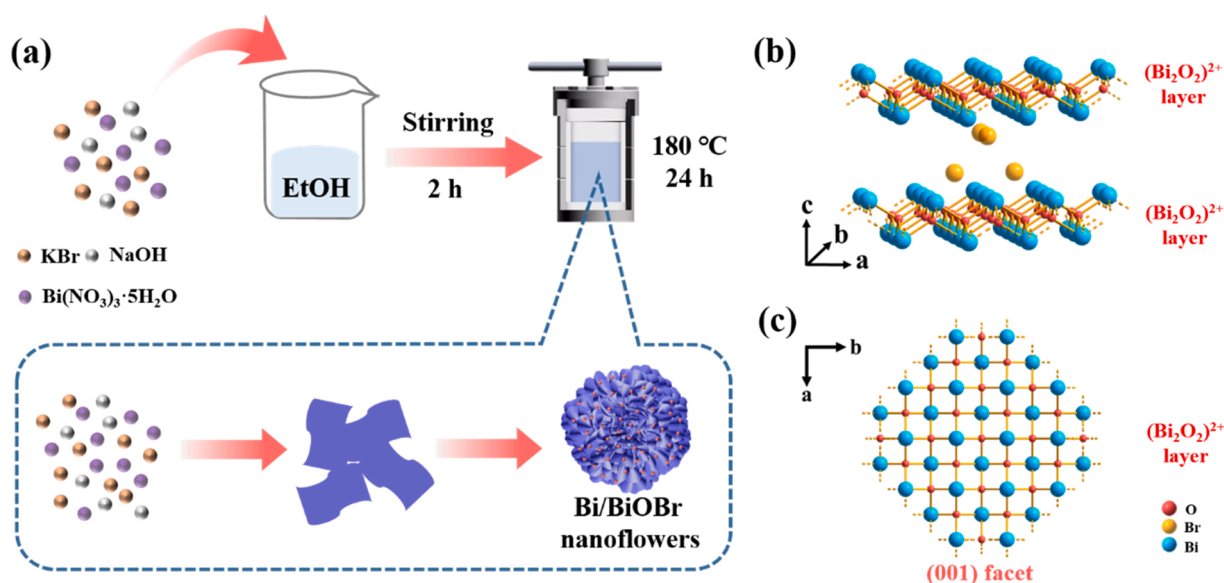


Fig. 1. (a) XRD patterns of as-prepared samples, (b-d) SEM images, (e) TEM and (f) SAED images of BOB-25.



Scheme 1. (a) Diagram of the possible formation mechanism of Bi/BiOBr nanoflowers, (b) the crystal structure of BiOBr along a-c and (c) a-b planes.

Fig. 1b-d, BOB-25 exhibits nanoflower morphology consisting of an abundance of nanosheets, and the average diameter of nanoflowers is about 1.5 μm. TEM was also used for the detailed description of the as-synthesized BOB-25 morphology, as shown in Fig. 1e. Two different types of lattice fringes are observed with d spacings of roughly 0.279 nm and 0.248 nm, which can be identified as the (104) and (004) planes of BiOBr. In addition, the interplanar spacing of 0.327 nm matches the (012) facet of metallic Bi well, which further verifies that metallic Bi is present on the surface of BOB-25 [19]. The selected area electron diffraction (SAED) image (Fig. 1f) demonstrates that the flower-like Bi/BiOBr is dominated with {010} facet.

Considering the results above, the formation mechanism of flower-like Bi/BiOBr was further discussed. The sheet-like BiOBr samples

were prepared with a mixed solvent of water and ethanol, while the flower-like Bi/BiOBr structures were obtained in a solvent of ethanol with sodium hydroxide (Fig. S3). The result indicates that the solvent ethanol and OH⁻ ions play a crucial part in the growth of the hierarchical nanoflowers. Initially, BiOBr nanoparticles are formed and then grow into nanosheets at the early stage. Furthermore, H⁺ ions absorb the terminated oxygen in the (Bi₂O₂)²⁺, thus preventing the growth rate of BiOBr along [010]. With the addition of sodium hydroxide, the binding interaction between H⁺ ions and terminated oxygen is reduced, promoting the growth of the (010) facet, thereby forming the BiOBr nanosheets [20]. Subsequently, ethanol acts as the structure-directing agent, directing the growth of BiOBr nanosheets into flower-like BiOBr [21]. Additionally, the distinctive hierarchical structure of the

nanoflowers can offer a substantial number of active sites and enhance the usage of light energy. The possible formation mechanism of Bi/BiOBr nanoflowers is shown in Scheme 1a. At the same time, part of the ethanol is oxidized into acetaldehyde, which can reduce BiOBr to metallic Bi in situ. As exhibited in Scheme 1b, BiOBr is made up of $(\text{Bi}_2\text{O}_2)^{2+}$ layers and Br^- , and the schematic diagrams of the crystal structure with the {001} projection of BiOBr is displayed in Scheme 1c.

3.2. Compositional information and optical properties

The XPS evaluation was further used to identify the chemical components and elucidate the chemical states of the components in BOB and BOB-25. According to Fig. S4a, XPS survey spectra of the samples indicate that BOB and BOB-25 consist of Bi, O and Br. Considering that Bi was easily oxidized in the air, the Bi 4f high-resolution XPS spectra over BOB-25 were characterized before and after argon ion etching. As illustrated in Fig. 2a, two peaks at 69.20 and 68.15 eV were detected and identified as Br $3d_{3/2}$ and $3d_{5/2}$, respectively [22]. The O 1s peaks in the high resolution XPS spectra (Fig. 2b) could be fitted by three peaks at 529.72, 530.81, and 532.49 eV, which may be due to the lattice oxygen, oxygen-related vacancies, the surface hydroxyl oxygen in the surface of BiOBr, respectively [23]. As shown in Fig. 2c, two intensive peaks at 158.99 and 164.30 eV correspond to the Bi $4f_{7/2}$ and Bi $4f_{5/2}$ spin-orbital components of Bi^{3+} in BOB. Compared to BOB, Bi 4f in BOB-25 shows a shift, stating the possibility of $\text{Bi}^{(3-x)+}$ appearance at the surface of BOB-25. The result may be attributed to the generation of defective sites around Bi^{3+} in $(\text{Bi}_2\text{O}_2)^{2+}$ [24]. Furthermore, two small peaks appeared at 156.87 and 162.22 eV after Ar-ion etching BOB-25, which were attributed to the metallic Bi [25]. The ESR technique was also employed to demonstrate the formation of oxygen vacancies. As illustrated in Fig. 2d, the signals at $g = 2.002$ associated with the character of oxygen vacancies can be detected for BOB and BOB-25 [26]. In addition, the signal of BOB-25 is obviously higher than that of BOB, suggesting that more oxygen vacancies are induced in BOB-25.

The UV-vis diffuse reflectance spectra (UV-vis DRS) were recorded to examine the light absorption capacity of the catalysts. As presented in Fig. 2e, the maximum absorption wavelength of BOB is around 430 nm as a result of the inherent band gap transition. Comparing with BOB, BOB-x displays a more powerful continuous absorption in the UV-Vis-NIR light region of 200–800 nm, which implies that the plasmonic Bi can facilitate light absorption via near-field enhancement-induced excitation mechanism [27]. The energy of optical band gap can be estimated further using the formula: $(\alpha h\nu)^{1/2} = A(h\nu - E_g)$, where α , $h\nu$, A and E_g represent the absorption coefficient, photon energy, a constant and band gap, respectively. The calculated optical band gap energies corresponding Tauc plots are about 2.83, 2.66, 2.49, 2.41, 2.41, and 2.39 eV for BOB, BOB-5, -10, -15, -20 and -25, respectively (Fig. 2f). The absorption edges of BOB-x exhibit a red-shift and the band gaps of BOB-x reduce with increasing ethanol contribution in the mixed solvent, which are due to the generation of oxygen vacancies [28]. According to the findings, the introduction of OVs and Bi nanoparticles allows the composites to absorb visible and near-infrared light photons. To investigate the impact of oxygen vacancies on band energy structure further, XPS valence band spectrum was performed to find the valence band maximum (VBM). As shown in Fig. S4b, the VBM values for BOB and BOB-25 are 2.00 and 2.03 eV, respectively. Combined with the band gap identified by UV-Vis DRS spectroscopy, the conduction band minimum (CBM) values of BOB and BOB-25 are deduced to be -0.83 and -0.36 eV, respectively.

3.3. Photocatalytic NO conversion

The photocatalytic activity of as-prepared samples toward ppb-NO removal was investigated under illumination of visible light ($\lambda \geq 420$ nm) in a continuous air flow glass reactor. As exhibited in Fig. 3a, the NO removal rates over BOB and BOB-25 are about 26 % and 63 %, respectively. Moreover, BOB-25 exhibits the best photocatalytic performance among the prepared materials. NO_2 , as a common

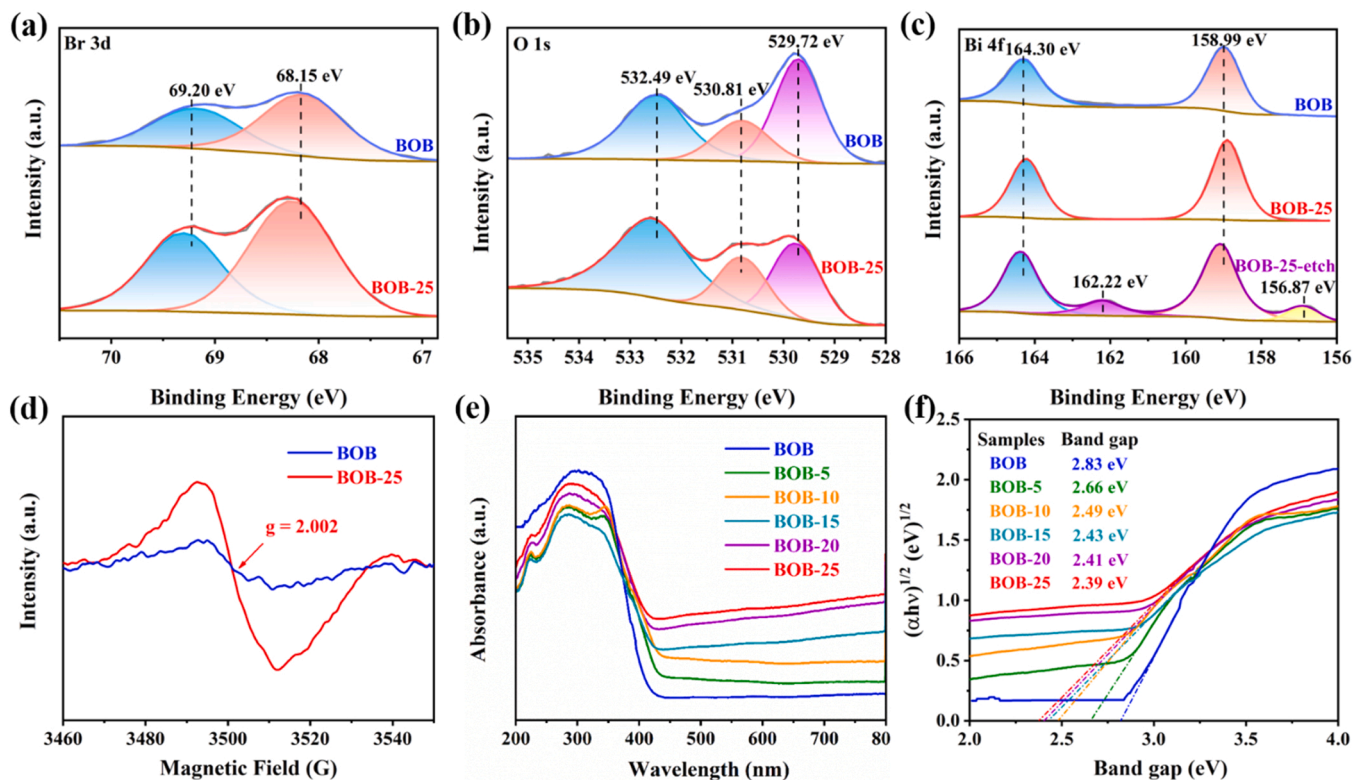


Fig. 2. The XPS spectra for (a) Br 3d, (b) O 1s and (c) Bi 4f of BOB and BOB-25; (d) The ESR spectra of BOB and BOB-25, (e) DRS spectra and (f) estimated bandgaps of as-prepared photocatalysts.

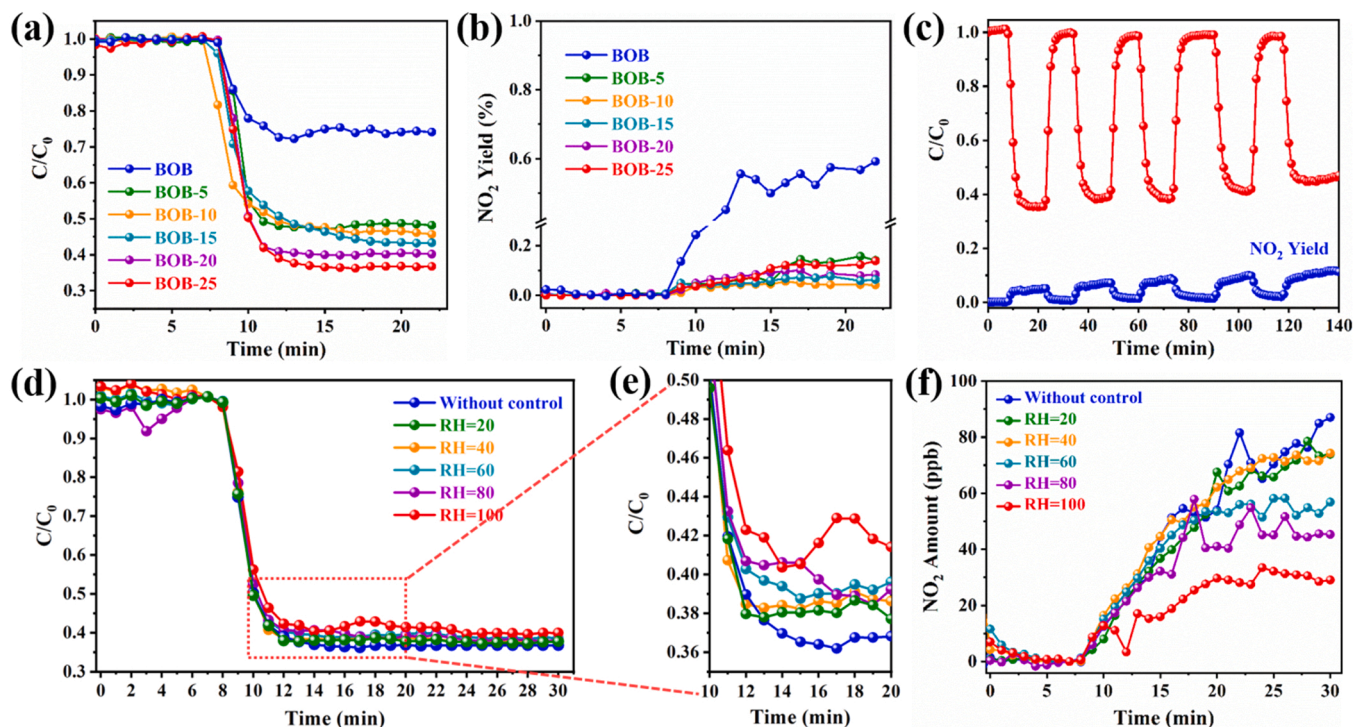


Fig. 3. (a) Photocatalytic NO conversion over a series of BOB-x ($x = 0, 5, 10, 15, 20$, and 25) samples under visible light, (b) the NO_2 formation yield following illumination with visible light, (c) multiple photocatalytic experiments over BOB-25, (d) photocatalytic NO conversion over BOB-25 and (e) its partial enlarged view, (f) the corresponding NO_2 production at various relative humidity levels.

intermediate, is shown to have higher toxicity than NO [29]. Therefore, how to minimize the generation of NO_2 in the process of NO photocatalytic conversion has been always remained a challenge. As exhibited in Fig. 3b, the NO_2 formation yield over BOB-25 reaches 7 %, which is significantly lower than 59 % of BOB. The improved photocatalytic efficiency of BOB-25 for removing NO with low NO_2 yield can be explained by the coexisted effects of plasmonic bismuth and oxygen vacancies. The subsequent photocatalytic removal tests were employed to explore the stability of BOB-25 for the NO removal. As shown in Fig. 3c, the NO removal rate over BOB-25 decreases smoothly following five cycles. After five cycles of NO photocatalytic removal, it is obvious that the crystalline phase of BOB-25 was negligibly changed (Fig. S6), implying that the BOB-25 photocatalyst has excellent stability. The role of water vapor during the photocatalytic conversion of NO cannot be ignored. Therefore, the photocatalytic removal efficiency over BOB-25 was evaluated at different relative humidity values ranging from 5 % to 100 % (the practical humidity of air used for photocatalytic NO removal was 5 % without control). According to Fig. 3d-f, the photocatalytic performance for NO removal indicates slight decrease with the increase of relative humidity. Furthermore, the surface hydrophilicity of as-prepared samples was further tested using a contact angle meter. As shown in Fig. S8, BOB-25 has a higher adsorption capacity for H_2O molecules compared with BOB, which is attributed to the presence of oxygen vacancies. The highly hydrophilic surface of BOB-25 facilitates competitive adsorption of gaseous NO and H_2O molecules. Therefore, the photocatalytic activity of BOB-25 slightly decreased with the increase of humidity. However, the amount of NO_2 decreases dramatically with the increase of relative humidity. Due to the high hydrophilicity of NO_2 , it may react with the H_2O molecules in the air. Considering the higher toxicity of NO_2 than NO, The De NO_x index (the detailed information was shown in Supporting Information) was employed to evaluate the photocatalytic NO removal performance over BOB-25 at various relative humidity levels. As shown in Fig. S9, the De NO_x index values of BOB-25 are positive, indicating that BOB-25 is suitable for the photocatalytic NO removal [30]. In addition, the De NO_x index of BOB-25 is

enhanced with the increasing relative humidity, implying that high relative humidity can suppress the production of toxic intermediate NO_2 .

3.4. Textural and photoelectrochemical properties

The N_2 adsorption-desorption isotherms and pore diameter distributions were performed to explore the surface characteristics of BOB and BOB-25. As shown in Fig. 4a and b, the both samples exhibit representative type IV adsorption-desorption isotherms. Meanwhile, the hysteresis loops at such a high relative pressure (between 0.6 and 1.0) can be assigned as the H3 type. The specific surface area of the flower-like BOB-25 is higher ($66.8 \text{ m}^2/\text{g}$) than that of pure BOB ($46.0 \text{ m}^2/\text{g}$), which is probably due to the use of ethanol, served as co-solvent. From Fig. 4b, the pore size distribution ranges from 5 to 130 nm. The most probable distributions for BOB and BOB-25 are $\sim 6 \text{ nm}$ and $\sim 9 \text{ nm}$, respectively, which is the characteristic of mesoporous materials.

Furthermore, the separation effectiveness of the photogenerated charges was characterized by photoluminescence spectrum (PL), time-resolved photoluminescence (TRPL) and photoelectrochemical measurements. As represented in Fig. 4c, the fluorescence intensity of BOB-25 is lower compared to pristine BOB, indicating that charge recombination has been significantly impeded by the formation of oxygen vacancies and plasmonic Bi [31]. Also, from Fig. 4d, the average fluorescence lifetimes (τ_{ave}) of BOB and BOB-25 are estimated to be 1.52 and 3.08 ns, respectively. The prolonged τ_{ave} value of BOB-25 suggests that the metallic bismuth and oxygen vacancies facilitate the efficient separation of the photogenerated carriers [32]. Meanwhile, BOB-25 exhibits a higher photocurrent response than pristine BOB under visible light irradiation (Fig. 4e), suggesting more efficient electron-hole separation [33]. The electrochemical impedance spectra (EIS) are shown in Fig. 4f. It is clear that BOB-25's Nyquist radius is smaller than that of BOB, which implies lower charge-transfer resistance (R_{ct}) in the interface of the semiconducting material [34]. The above results further verify that the formation of oxygen vacancies and metallic Bi is essential

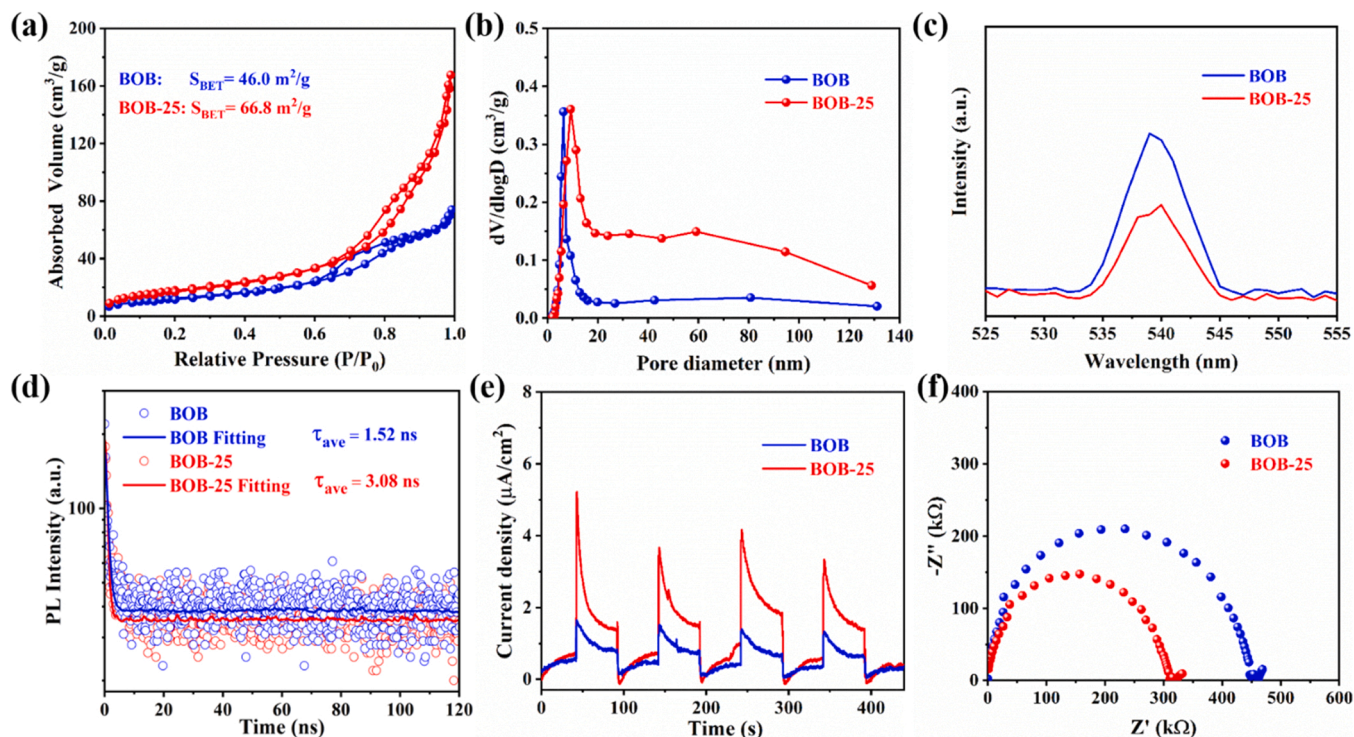


Fig. 4. (a) The isotherms of N_2 adsorption-desorption and (b) the curves of pore-size distribution for BOB and BOB-25, (c) the photoluminescence spectra, (d) time-resolved photoluminescence spectrum, (e) transient photocurrent responses and (f) electrochemical impedance spectra of BOB and BOB-25.

in increasing BOB-25's photocatalytic activity.

3.5. The co-effect of Bi and OV on the generation of reactive oxygen species

It is important to explore the formation process of active radicals for further revealing the photocatalytic mechanism of the reaction. Accordingly, the ESR testings were carried out to track the active radicals produced by BOB and BOB-25 under visible light. As shown in Fig. 5a and b, no ESR signals were observed in dark. Meanwhile, four peaks with the relative intensity of 1:1:1:1 were detected after 5 min of light irradiation for both BOB and BOB-25, which are assigned to the superoxide radical ($\bullet O_2^-$) [35]. From Fig. 5b, the relative intensity of hydroxyl radical ($\bullet OH$) signals, which are produced from the oxidation of adsorbed OH^- by photogenerated h^+ on the surface of BOB and BOB-25, is 1:2:2:1 [36]. Additionally, the enhanced $\bullet O_2^-$ and $\bullet OH$ signals of BOB-25 can be due to the synergy of Bi and OVs, which can expedite the photogenerated charges separation and transport.

The undeniable role of ROS engaged in the photocatalytic NO removal over BOB-25 was further explored by adding a series of scavenging agents to the photoreaction medium. $\bullet O_2^-$, $\bullet OH$, e^- and h^+ were trapped using p-benzoquinone (p-BQ), tertbutyl alcohol (TBA), potassium dichromate ($K_2Cr_2O_7$) and potassium iodide (KI), respectively. As depicted in Fig. 5c, the addition of $K_2Cr_2O_7$, p-BQ and KI significantly reduces the photocatalytic efficiency, confirming that e^- , $\bullet O_2^-$ and h^+ are essential in the photocatalytic process. According to the findings of these experiments and ESR characterization, a plausible photocatalytic mechanism is proposed (Fig. 5d). Firstly, when the energy of the illuminating photons surpasses the bandgap of BOB-25, electrons transit from the valence band (VB) to the conduction band (CB), accompanied with the generation of photogenerated holes. The photogenerated charges react with the adsorbed O_2 and H_2O on the photocatalyst surfaces to produce reactive oxygen species including $\bullet O_2^-$ and $\bullet OH$. Meanwhile, the plasmonic Bi with a larger work function than BiOBr can serve as an electron sink and trap photo-induced electrons during

photocatalytic processes, which inhibits the recombination of photoinduced charge carriers [37]. The equation $E_{CB} = E_{VB} - E_g$ can be used to calculate the CB edge of BOB-25 ($E_{CB} = -0.36$ eV). Since the redox potential of $OH^-/\bullet OH$ (1.99 eV) is more negative than the VB of BiOBr (2.03 eV), h^+ left in the VB of BiOBr could trigger the production of $\bullet OH$ [38]. In addition, the CB potential of BOB-25 (-0.36 eV) is sufficiently negative to perform the single-electron reduction of O_2 to $\bullet O_2^-$ [39]. As reported, the impurity level can be formed between VB and CB because of the presence of oxygen vacancies, which could prevent photo-generated electron-hole pairs from recombination [25].

3.6. TPD measurements and in situ DRIFTS -analysis of the NO conversion pathway

The adsorption of O_2 and NO on photocatalyst surface is prerequisite for the production of ROS and NO removal. To demonstrate the O_2 and NO adsorption performance on BOB and BOB-25, the temperature-programmed desorption (TPD) analysis was carried out. The O_2 -TPD curves, according to Fig. 6a, can be separated into three regions: low, medium, and high temperatures, which typically correspond to physical oxygen adsorption, superoxide species adsorption and lattice oxygen release, respectively [40]. Oxygen desorption in the middle temperature zone (300–500 °C) is commonly corresponded to the formed $\bullet O_2^-$ on OVs [41]. In particular, the peak area of $\bullet O_2^-$ desorption on BOB-25 is remarkably larger, especially in the medium-temperature zone, than BOB, which implies higher O_2 adsorption capacity on BOB-25. From the NO-TPD profiles of BOB and BOB-25, Fig. 6b, there is a peak centered at ~ 147 °C, which is assigned to the physisorption of NO [42]. In comparison to pristine BOB, the peak intensity at ~ 422 °C is much stronger for BOB-25, suggesting its strong NO adsorption performance. The oxygen vacancies formed on the surface of BOB-25 can serve as Lewis acid sites, accelerating the adsorption of NO as a Lewis base.

In situ DRIFTS spectra were performed to provide further mechanistic description of the NO photocatalytic oxidation over pristine BOB and BOB-25. To clearly observe the transition of intermediate products

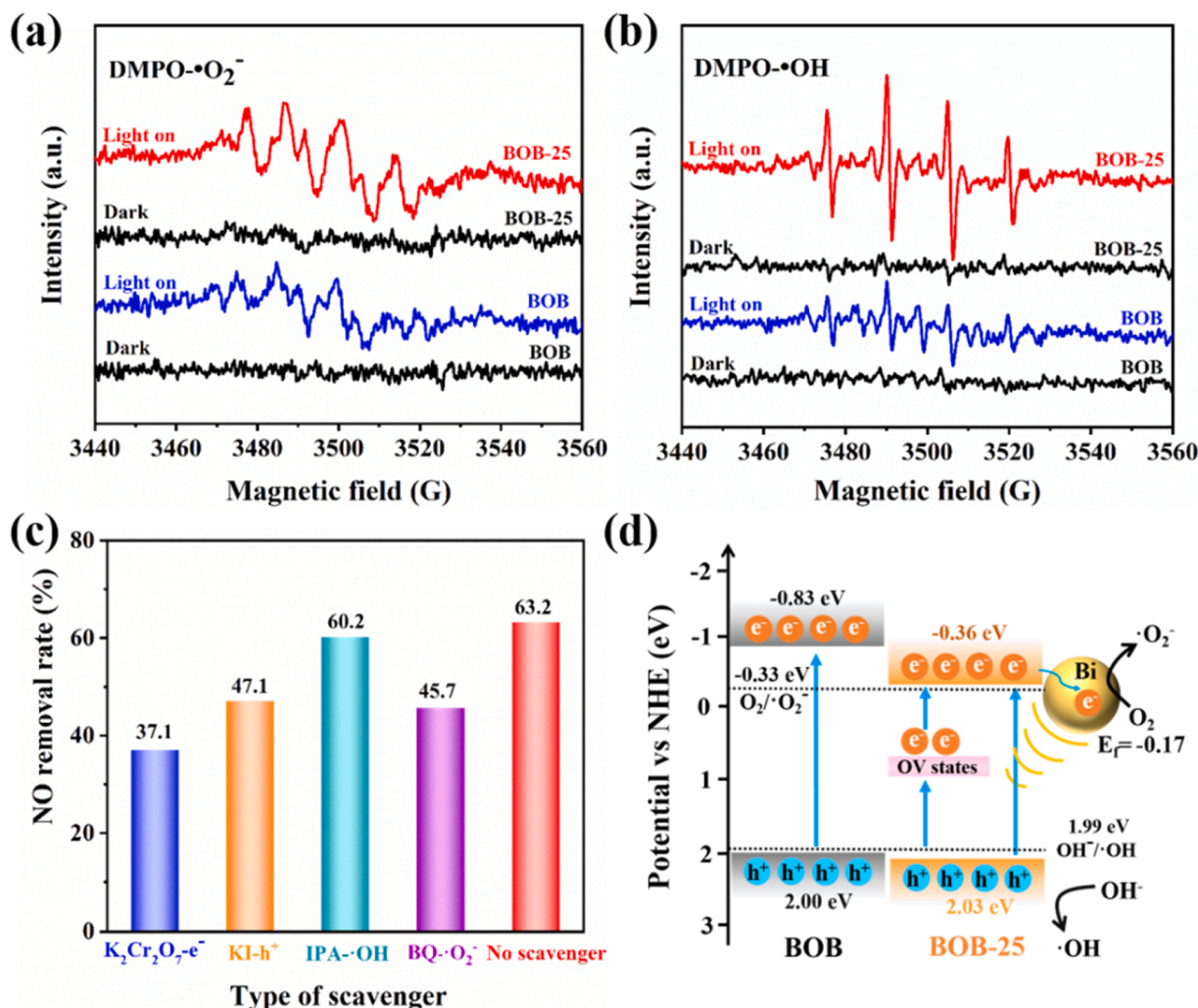


Fig. 5. The ESR -spectra of (a) $\cdot\text{O}_2^-$ and (b) $\cdot\text{OH}$ in darkness and under visible light irradiation, (c) the scavenging experiments over BOB-25 and (d) the plausible schematic diagram for ROS generation under visible light.

during the photocatalytic reaction, the equilibrium state of the samples under helium atmosphere was employed as the reference. The time-dependent characteristic peaks of NO and intermediates throughout the process of adsorption and NO photocatalytic removal are exhibited in Fig. 6c and d. After reaching the adsorption equilibrium of NO at dark, two bands at 1515 and 1642 cm^{-1} were detected, which are considered as the characteristic peaks of NO [43]. Moreover, the absorption bands at 2890, 2953 and 2982 cm^{-1} can be corresponded to NO_2 , indicating that a portion of NO is slowly oxidized to NO_2 by O_2 [44]. Longer exposure time results in the attenuation of NO peak and increase of NO_2 peak intensity, indicating that part of NO is converted to NO_2 by active species. Furthermore, the appearance of peaks at 1276 cm^{-1} and some other weakly characteristic absorption peaks imply the emergence of new species on the surface of BOB, such as monodentate NO_3^- at 1486 cm^{-1} , monodentate NO_2^- (1000–1150, 1314 and 1336 cm^{-1}) and nitro compound (976 and 1362 cm^{-1}) [45,46]. Compared to BOB, there is an obvious absorption peak at 1649 cm^{-1} , indicating that BOB-25 has stronger adsorption of NO, which agrees with the NO-TPD results. The outcome further verifies that oxygen vacancies play a key role in NO adsorption. Moreover, the appearance of a strong NO_2 absorption peak at 1629 cm^{-1} declares that NO reacts with a large amount of oxygen adsorbed at the oxygen vacancies (Fig. S7). The NOH intermediates were also detected on both samples, probably due to the reaction of NO with surface hydroxyl group (1117 cm^{-1}) [47]. After turning on the lamp, the IR bands of NO_2 exhibit a gradually decreasing trend with the irradiation

time. At the same time, a considerable number of nitrate and nitrite species appear on the surface of BOB-25. These peaks grow increasingly discernible with irradiation time, indicating that NO_2 has been further deeply oxidized into nitrate and nitrite species. Particularly the new peaks at 1543 cm^{-1} are assigned to the bridging nitrates, which are more stable than monodentate nitrates [48]. Moreover, intermediates of NO^+ can be detected at 2186 cm^{-1} , meaning that the oxygen vacancies adsorb the outer layer electrons of NO [49]. These findings suggest that additional active sites are successfully generated on BOB-25 for the adsorption and photocatalytic oxidation of NO, leading to the enhanced NO photocatalytic removal efficiency. Table 1 lists the main detected IR bands of the adsorbed species as well as their chemical designations.

The potential NO adsorption and photocatalytic conversion routes on the catalyst surface are illustrated in Fig. 7. First, the oxygen atoms in BOB-25 establish hydrogen bonds with water molecules in the air. The O_2 and NO molecules are then adsorbed onto the oxygen vacancies and hydrogen bonds. H_2O molecules subsequently depart from the catalyst surface, which leads to the emergence of unstable intermediates. Following that, under the synergistic influence of reactive oxygen species and water molecules in the air, the produced intermediates undergo the transition of NO to the monodentate nitrate and bridging nitrate. After removing the nitrate ions, the catalyst reaches its initial state, allowing the exposed active site to once again adsorb the unreacted gas. It is worth mentioning that, in addition to this primary reaction pathway, NO_2 gas molecules could also be detached from the unstable

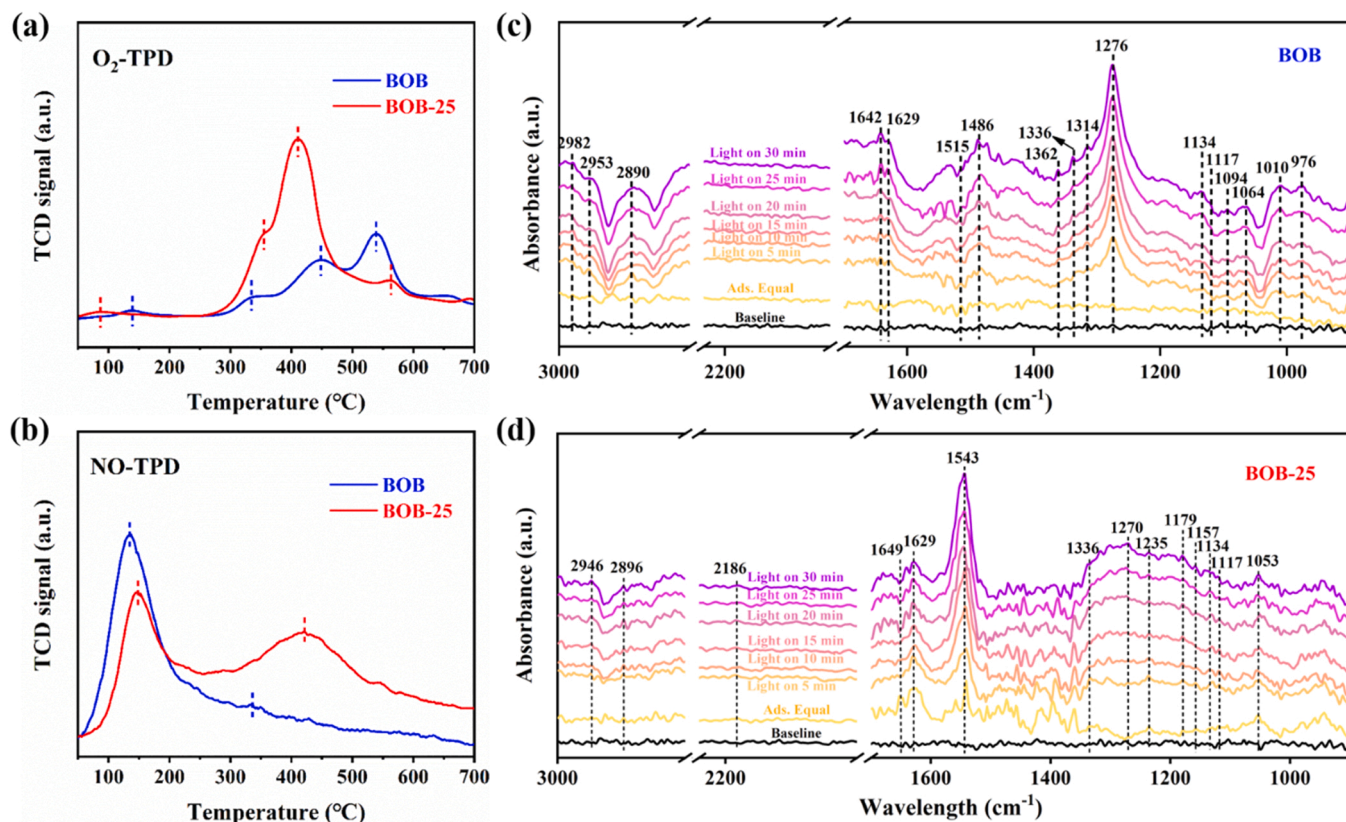


Fig. 6. (a) The O₂-TPD spectra and (b) NO-TPD spectra of BOB and BOB-25, the time-dependent in situ NO DRIFT spectra over (c) BOB and (d) BOB-25 during photocatalytic NO removal.

Table 1

The IR band assignments for the processes of photocatalytic NO oxidation over BOB and BOB-25.

Wavenumbers (cm ⁻¹)	Assignment	References
976	N ₂ O ₃	[46]
1010, 1120–1150, 1314, 1336	Monodentate NO ₂ ⁻	[50]
1117	NOH	[47]
1150–1280, 1486	Monodentate NO ₃ ⁻	[45]
1362	Hyponitrite N ₂ O ₂ ⁻	[51]
1543	Bridging NO ₃ ⁻	[48]
1515, 1642, 1649	NO	[43]
2186	NO ⁺	[49]
1629, 2800–3000	NO ₂	[44]

intermediate surface and react directly with H₂O molecules in the air to form nitric acid, which inhibits the production of toxic NO₂ and facilitates the deep oxidation of NO. Based on the trapping experiments and in situ DRIFTS results, the photocatalytic pathway of NO removal over BOB-25 is described as following (Eqs. 1–12):

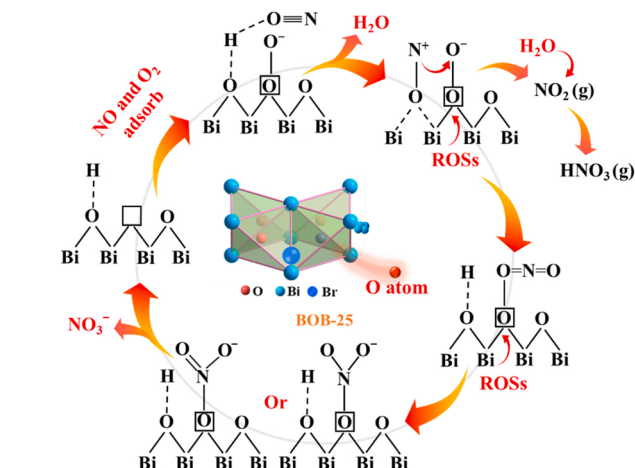
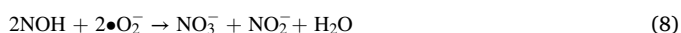
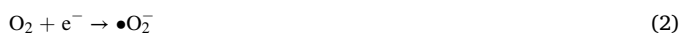


Fig. 7. The proposed NO adsorption and photocatalytic conversion routes over BOB-25.



4. Conclusions

High-performance defective Bi/BiOBr nanoflowers were successfully fabricated by a solvothermal method. The interaction between OV and Bi enhanced the photocatalytic performance of BiOBr towards NO removal under visible light and BOB-25 showed the highest efficiency, 63 %, with a low NO₂ generation. The photocatalytic pathway and mechanism were further revealed by in-situ DRFTS. More importantly, the performance test results at various relative humidity levels showed that the adsorption of gaseous NO molecules was barely affected by water molecules. However, the presence of H₂O molecules promoted the conversion of toxic NO₂ intermediate to nitrate. This work is prone to provide insights for the photocatalytic NO removal by deep oxidation of NO through relative humidity control.

CRediT authorship contribution statement

Yue Xin and Qiuhui Zhu contributed equally to this work. **Yue Xin:** Conceptualization, Investigation, Methodology, Validation, Visualization, Data curation, Writing – original draft. **Qiuhui Zhu:** Conceptualization, Investigation, Methodology, Validation, Visualization, Data curation, Writing – original draft; **Ting Gao:** Writing – review & editing, Visualization. **Ximing Li:** Writing – review & editing, Visualization. **Wei Zhang:** Writing – review & editing. **Hui Wang:** Writing – review & editing; **Donghang Ji:** Investigation, Validation; **Yu Huang:** Investigation, Resources. **Mohsen Padervand:** Project administration, Visualization, Writing – review & editing. **Feng Yu:** Supervision, Writing – review & editing. **Chuanyi Wang:** Conceptualization, Visualization, Supervision, Resources, Project administration, Writing – review & editing.

Declaration of Competing Interest

The authors declare that they have no known competing financial interests or personal relationships that could have appeared to influence the work reported in this paper.

Data Availability

No data was used for the research described in the article.

Acknowledgments

This work was supported by the National Natural Science Foundation of China (Nos. 52161145409, 21976116), Shaanxi Science and Technology Program (2020KWZ-005), Foreign Expert Project of SAFEA of China (DL2021041001L and QN2021041003L), Alexander-von-Humboldt Foundation of Germany (Group-Linkage Program), and Iranian National Science Foundation (Grant No. 4001153).

References

- [1] T.H. Huy, D.P. Bui, F. Kang, Y. Wang, S. Liu, C.M. Thi, S. You, G. Chang, V. Pham, SnO₂/TiO₂ nanotube heterojunction: the first investigation of NO degradation by visiblelight-driven photocatalysis, *Chemosphere* 215 (2019) 323–332, <https://doi.org/10.1016/j.chemosphere.2018.10.033>.
- [2] Y. Duan, J. Luo, S. Zhou, X. Mao, M.W. Shah, F. Wang, Z. Chen, C. Wang, TiO₂-supported Ag nanoclusters with enhanced visible light activity for the photocatalytic removal of NO, *Appl. Catal. B* 234 (2018) 206–212, <https://doi.org/10.1016/j.apcatb.2018.04.041>.
- [3] H.R.S. Abdellatif, G. Zhang, Y. Tang, W. Ruan, J. Li, D. Xie, J. Ni, C. Ni, A highly efficient dual-phase GaN(O)/Nb₂O₅(N) photocatalyst prepared through nitridation and reoxidation process for NO removal, *Chem. Eng. J.* 402 (2020), 126199, <https://doi.org/10.1016/j.cej.2020.126199>.
- [4] N. Li, M. Shi, Y. Xin, W. Zhang, J. Qin, K. Zhang, H. Lv, M. Yuan, C. Wang, Oxygen vacancies-modified S-scheme Bi₂Ti₂O₇/CaTiO₃ heterojunction for highly efficient photocatalytic NO removal under visible light, *J. Environ. Chem. Eng.* 10 (3) (2022), 107420, <https://doi.org/10.1016/j.jece.2022.107420>.
- [5] Y. Jing, A. Fan, J. Guo, T. Shen, S. Yuan, Y. Chu, Synthesis of an ultrathin MnO₂ nanosheet-coated Bi₂WO₆ nanosheet as a heterojunction photocatalyst with enhanced photocatalytic activity, *Chem. Eng. J.* 429 (2022), 132193, <https://doi.org/10.1016/j.cej.2021.132193>.
- [6] A. Fujishima, K. Honda, Electrochemical photolysis of water at a semiconductor electrode, *Nature* 238 (1972) 37–38, <https://doi.org/10.1038/238037a0>.
- [7] Q. Zhu, K. Zhang, D. Li, N. Li, J. Xu, D.W. Bahnemann, C. Wang, Polarization-enhanced photocatalytic activity in non-centrosymmetric materials based photocatalysis: a review, *Chem. Eng. J.* 426 (2021), <https://doi.org/10.1016/j.cej.2021.131681>.
- [8] J. Sha, L. Li, Z. An, M. He, H. Yu, Y. Wang, B. Gao, S. Xu, Diametrically opposite effect of Cu²⁺ on sulfamerazine and ciprofloxacin adsorption-photodegradation in g-C₃N₄/visible light system: behavior and mechanism study, *Chem. Eng. J.* 428 (2022), <https://doi.org/10.1016/j.cej.2021.131065>.
- [9] N. Li, C. Wang, K. Zhang, H. Lv, M. Yuan, D.W. Bahnemann, Progress and prospects of photocatalytic conversion of low-concentration NO_x, *Chin. J. Catal.* 43 (9) (2022) 2363–2387, [https://doi.org/10.1016/s1872-2067\(22\)64139-1](https://doi.org/10.1016/s1872-2067(22)64139-1).
- [10] Y. Jin, F. Li, T. Li, X. Xing, W. Fan, L. Zhang, C. Hu, Enhanced internal electric field in S-doped BiOBr for intercalation, adsorption and degradation of ciprofloxacin by photoinitiation, *Appl. Catal. B* 302 (2022), 120824, <https://doi.org/10.1016/j.apcatb.2021.120824>.
- [11] J. Ni, D. Liu, W. Wang, A. Wang, J. Jia, J. Tian, Z. Xing, Hierarchical defect-rich flower-like BiOBr/Ag nanoparticles/ultrathin g-C₃N₄ with transfer channels plasmonic Z-scheme heterojunction photocatalyst for accelerated visible-light-driven photothermal-photocatalytic oxytetracycline degradation, *Chem. Eng. J.* 419 (2021), 129969, <https://doi.org/10.1016/j.cej.2021.129969>.
- [12] F. Wang, Y. Wang, Y. Feng, Y. Zeng, Z. Xie, Q. Zhang, Y. Su, P. Chen, Y. Liu, K. Yao, W. Lv, G. Liu, Novel ternary photocatalyst of single atom-dispersed silver and carbon quantum dots co-loaded with ultrathin g-C₃N₄ for broad spectrum photocatalytic degradation of naproxen, *Appl. Catal. B* 221 (2018) 510–520, <https://doi.org/10.1016/j.apcatb.2017.09.055>.
- [13] G. Liu, Y. Huang, H. Lv, H. Wang, Y. Zeng, M. Yuan, Q. Meng, C. Wang, Confining single-atom Pd on g-C₃N₄ with carbon vacancies towards enhanced photocatalytic NO conversion, *Appl. Catal. B* 284 (2021), <https://doi.org/10.1016/j.apcatb.2020.119683>.
- [14] Q. Zhu, R. Hailili, Y. Xin, Y. Zhou, Y. Huang, X. Pang, K. Zhang, P.K.J. Robertson, D.W. Bahnemann, C. Wang, Efficient full spectrum responsive photocatalytic NO conversion at Bi₂Ti₂O₇: co-effect of plasmonic Bi and oxygen vacancies, *Appl. Catal. B* 319 (2022), 121888, <https://doi.org/10.1016/j.apcatb.2022.121888>.
- [15] Q. Zhu, A.A. Dar, Y. Zhou, K. Zhang, J. Qin, B. Pan, J. Lin, A.O.T. Patrocínio, C. Wang, Oxygen Vacancies Promoted Piezoelectricity toward Piezo-Photocatalytic Decomposition of Tetracycline over SrBi₄Ti₄O₁₅, *ACS ES&T. Eng.*, <https://doi.org/10.1021/acsestengg.1c00479>.
- [16] Y. Li, M. Wen, Y. Wang, G. Tian, C. Wang, J. Zhao, Plasmonic hot electrons from oxygen vacancies for infrared light-driven catalytic CO₂ reduction on BiO_{3-x}, *Angew. Chem. Int. Ed.* 60 (2) (2021) 910–916, <https://doi.org/10.1002/anie.202010156>.
- [17] L. Hao, H. Huang, Y. Zhang, T. Ma, Oxygen vacant semiconductor photocatalysts, *Adv. Funct. Mater.* 31 (2021), <https://doi.org/10.1002/adfm.202100919>.
- [18] M. Gu, Y. Li, M. Zhang, X. Zhang, Y. Shen, Y. Liu, F. Dong, Bismuth nanoparticles and oxygen vacancies synergistically attired Zn₂SnO₄ with optimized visible-light-active performance, *Nano Energy* 80 (2021), 105415, <https://doi.org/10.1016/j.nanoen.2020.105415>.
- [19] X. Xue, R. Chen, H. Chen, Y. Hu, Q. Ding, Z. Liu, L. Ma, G. Zhu, W. Zhang, Q. Yu, J. Liu, J. Ma, Z. Jin, Oxygen vacancy engineering promoted photocatalytic ammonia synthesis on ultrathin two-dimensional bismuth oxybromide nanosheets, *Nano Lett.* 18 (11) (2018) 7372–7377, <https://doi.org/10.1021/acs.nanolett.8b03655>.
- [20] X. Xiong, L. Ding, Q. Wang, Y. Li, Q. Jiang, J. Hu, Synthesis and photocatalytic activity of BiOBr nanosheets with tunable exposed {010} facets, *Appl. Catal. B* 188 (2016) 283–291, <https://doi.org/10.1016/j.apcatb.2016.02.018>.
- [21] X. Zhang, Z. Ai, F. Jia, L. Zhang, Generalized one-pot synthesis, characterization, and photocatalytic activity of hierarchical BiOX (X = Cl, Br, I) nanoplate microspheres, *J. Phys. Chem. C* 112 (3) (2008) 747–753, <https://doi.org/10.1021/jp077471t>.
- [22] J. Sun, X. Li, Q. Zhao, B. Liu, Ultrathin nanoflake-assembled hierarchical BiOBr microflower with highly exposed {001} facets for efficient photocatalytic degradation of gaseous ortho-dichlorobenzene, *Appl. Catal. B* 281 (2021), 119478, <https://doi.org/10.1016/j.apcatb.2020.119478>.
- [23] H. Wang, D. Yong, S. Chen, S. Jiang, X. Zhang, W. Shao, Q. Zhang, W. Yan, B. Pan, Y. Xie, Oxygen-vacancy-mediated exciton dissociation in BiOBr for boosting charge-carrier-involved molecular oxygen activation, *J. Am. Chem. Soc.* 140 (5) (2018) 1760–1766, <https://doi.org/10.1021/jacs.7b10997>.
- [24] Y. Guo, Y. Zhang, N. Tian, H. Huang, Homogeneous {001}-BiOBr/Bi heterojunctions: facile controllable synthesis and morphology-dependent photocatalytic activity, *ACS Sustain. Chem. Eng.* 4 (7) (2016) 4003–4012, <https://doi.org/10.1021/acssuschemeng.6b00884>.
- [25] W. He, Y. Sun, G. Jiang, Y. Li, X. Zhang, Y. Zhang, Y. Zhou, F. Dong, Defective Bi₄MoO₉/Bi metal core/shell heterostructure: enhanced visible light photocatalysis and reaction mechanism, *Appl. Catal. B* 239 (2018) 619–627, <https://doi.org/10.1016/j.apcatb.2018.08.064>.
- [26] Y. Bu, H. Li, W. Yu, Y. Pan, L. Li, Y. Wang, L. Pu, J. Ding, G. Gao, B. Pan, Peroxydisulfate activation and singlet oxygen generation by oxygen vacancy for degradation of contaminants, *Environ. Sci. Technol.* 55 (3) (2021) 2110–2120, <https://doi.org/10.1021/acs.est.0c07274>.
- [27] R.K. Chava, N. Son, M. Kang, Bismuth quantum dots anchored one-dimensional CdS as plasmonic photocatalyst for pharmaceutical tetracycline hydrochloride

- pollutant degradation, *Chemosphere* 300 (2022), <https://doi.org/10.1016/j.chemosphere.2022.134570>.
- [28] H. Yu, J. Huang, L. Jiang, Y. Shi, K. Yi, W. Zhang, J. Zhang, H. Chen, X. Yuan, Enhanced photocatalytic tetracycline degradation using N-CQDs/OV-BiOBr composites: unraveling the complementary effects between N-CQDs and oxygen vacancy, *Chem. Eng. J.* 402 (2020), <https://doi.org/10.1016/j.cej.2020.126187>.
- [29] Q. Zhang, Y. Huang, L. Xu, J. Cao, W. Ho, S.C. Lee, Visible-light-active plasmonic Ag-SrTiO₃ nanocomposites for the degradation of NO in air with high selectivity, *ACS Appl. Mater. Interfaces* 8 (6) (2016) 4165–4174, <https://doi.org/10.1021/acsami.5b11887>.
- [30] E. Ebrahimi, M. Irfan, F. Shabani, Y. Kocak, B. Karakurt, E. Erdem, H.V. Demir, E. Ozensoy, Core-crown quantum nanoplatelets with favorable type-II heterojunctions boost charge separation and photocatalytic NO oxidation on TiO₂, *Chemcatchem* 12 (24) (2020) 6329–6343, <https://doi.org/10.1002/cctc.202000749>.
- [31] P. Chen, H. Liu, Y. Sun, J. Li, W. Cui, L. Wang, W. Zhang, X. Yuan, Z. Wang, Y. Zhang, F. Dong, Bi metal prevents the deactivation of oxygen vacancies in Bi₂O₂CO₃ for stable and efficient photocatalytic NO abatement, *Appl. Catal. B* 264 (2020), 118545, <https://doi.org/10.1016/j.apcatb.2019.118545>.
- [32] D. Majhi, K. Das, A. Mishra, R. Dhiman, B.G. Mishra, One pot synthesis of CdS/BiOBr/Bi₂O₂CO₃: a novel ternary double Z-scheme heterostructure photocatalyst for efficient degradation of atrazine, *Appl. Catal. B* 260 (2020), <https://doi.org/10.1016/j.apcatb.2019.118222>.
- [33] Z. Long, G. Zhang, H. Du, J. Zhu, J. Li, Preparation and application of BiOBr-Bi₂S₃ heterojunctions for efficient photocatalytic removal of Cr(VI), *J. Hazard. Mater.* 407 (2021), <https://doi.org/10.1016/j.jhazmat.2020.124394>.
- [34] M. Xu, X. Jiang, J. Li, F. Wang, K. Li, X. Cheng, Self-assembly of a 3D hollow BiOBr@Bi-MOF heterostructure with enhanced photocatalytic degradation of dyes, *ACS Appl. Mater. Interfaces* 13 (47) (2021) 56171–56180, <https://doi.org/10.1021/acsami.1c16612>.
- [35] M. Kou, Y. Deng, R. Zhang, L. Wang, P. Wong, F. Su, L. Ye, Molecular oxygen activation enhancement by BiOBr_{0.5}I_{0.5}/BiOI utilizing the synergistic effect of solid solution and heterojunctions for photocatalytic NO removal, *Chin. J. Catal.* 41 (10) (2020) 1480–1487, [https://doi.org/10.1016/s1872-2067\(20\)63607-5](https://doi.org/10.1016/s1872-2067(20)63607-5).
- [36] G. Qin, H. Xie, H. Ye, Y. Sun, X. Hou, Z. Wang, D. Fan, Atomic interfacial structure and charge transfer mechanism on in-situ formed BiOI/Bi₂O₂SO₄ p-n heterojunctions with highly promoted photocatalysis, *Appl. Catal. B* 297 (2021), <https://doi.org/10.1016/j.apcatb.2021.120492>.
- [37] H. Wang, W. Zhang, X. Li, J. Li, W. Cen, Q. Li, F. Dong, Highly enhanced visible light photocatalysis and in situ FT-IR studies on Bi metal@defective BiOI hierarchical microspheres, *Appl. Catal. B* 225 (2018) 218–227, <https://doi.org/10.1016/j.apcatb.2017.11.079>.
- [38] F. Dong, Q. Li, Y. Sun, W.K. Ho, Noble metal-like behavior of plasmonic Bi particles as a cocatalyst deposited on (BiO)₂CO₃ microspheres for efficient visible light photocatalysis, *ACS Catal.* 4 (12) (2014) 4341–4350, <https://doi.org/10.1021/cs501038q>.
- [39] X. Li, J. Xiong, X. Gao, J. Ma, Z. Chen, B. Kang, J. Liu, H. Li, Z. Feng, J. Huang, Novel BP/BiOBr S-scheme nano-heterojunction for enhanced visible-light photocatalytic tetracycline removal and oxygen evolution activity, *J. Hazard. Mater.* 387 (2020), <https://doi.org/10.1016/j.jhazmat.2019.121690>.
- [40] H. Shang, M. Li, H. Li, S. Huang, C. Mao, Z. Ai, L. Zhang, Oxygen vacancies promoted the selective photocatalytic removal of NO with blue TiO₂ via simultaneous molecular oxygen activation and photogenerated hole annihilation, *Environ. Sci. Technol.* 53 (11) (2019) 6444–6453, <https://doi.org/10.1021/acs.est.8b07322>.
- [41] H. Shang, S. Huang, H. Li, M. Li, S. Zhao, J. Wang, Z. Ai, L. Zhang, Dual-site activation enhanced photocatalytic removal of NO with Au/CeO₂, *Chem. Eng. J.* 386 (2020), <https://doi.org/10.1016/j.cej.2020.124047>.
- [42] Y. Lu, Y. Huang, Y. Zhang, J. Cao, H. Li, C. Bian, S.C. Lee, Oxygen vacancy engineering of Bi₂O₃/Bi₂O₂CO₃ heterojunctions: Implications of the interfacial charge transfer, NO adsorption and removal, *Appl. Catal. B* 231 (2018) 357–367, <https://doi.org/10.1016/j.apcatb.2018.01.008>.
- [43] Q. Li, S. Gao, J. Hu, H. Wang, Z. Wu, Superior NO_x photocatalytic removal over hybrid hierarchical Bi/BiOI with high non-NO₂ selectivity: synergistic effect of oxygen vacancies and bismuth nanoparticles, *Catal. Sci. Technol.* 8 (20) (2018) 5270–5279, <https://doi.org/10.1039/c8cy01466c>.
- [44] H. Wu, C. Yuan, R. Chen, J. Wang, F. Dong, J. Li, Y. Sun, Mechanisms of interfacial charge transfer and photocatalytic NO oxidation on BiOBr/SnO₂ p-n heterojunctions, *ACS Appl. Mater. Interfaces* 12 (39) (2020) 43741–43749, <https://doi.org/10.1021/acsami.0c12628>.
- [45] W. He, Y. Sun, G. Jiang, H. Huang, X. Zhang, F. Dong, Activation of amorphous Bi₂WO₆ with synchronous Bi metal and Bi₂O₃ coupling: photocatalysis mechanism and reaction pathway, *Appl. Catal. B* 232 (2018) 340–347, <https://doi.org/10.1016/j.apcatb.2018.03.047>.
- [46] Y. Wang, K. Wang, J. Wang, X. Wu, G. Zhang, Sb₂WO₆/BiOBr 2D nanocomposite S-scheme photocatalyst for NO removal, *J. Mater. Sci. Technol.* 56 (2020) 236–243, <https://doi.org/10.1016/j.jmst.2020.03.039>.
- [47] M. Kantcheva, Identification, stability, and reactivity of NO_x species adsorbed on titania-supported manganese catalysts, *J. Catal.* 204 (2) (2001) 479–494, <https://doi.org/10.1006/jcat.2001.3413>.
- [48] Q. Geng, H. Xie, W. Cui, J. Sheng, X. Tong, Y. Sun, J. Li, Z. Wang, F. Dong, Optimizing the electronic structure of BiOBr nanosheets via combined Ba doping and oxygen vacancies for promoted photocatalysis, *J. Phys. Chem. C* 125 (16) (2021) 8597–8605, <https://doi.org/10.1021/acs.jpcc.1c00772>.
- [49] W. He, Y. Sun, G. Jiang, Y. Li, X. Zhang, Y. Zhang, Y. Zhou, F. Dong, Defective Bi₄MoO₉/Bi metal core/shell heterostructure: enhanced visible light photocatalysis and reaction mechanism, *Appl. Catal. B* 239 (2018) 619–627, <https://doi.org/10.1016/j.apcatb.2018.08.064>.
- [50] H. Wu, R. Chen, H. Wang, W. Cui, J. Li, J. Wang, C. Yuan, L. Zhuo, Y. Zhang, F. Dong, An atomic insight into BiOBr/La₂Ti₂O₇ p-n heterojunctions: interfacial charge transfer pathway and photocatalysis mechanism, *Catal. Sci. Technol.* 10 (3) (2020) 826–834, <https://doi.org/10.1039/c9cy02230a>.
- [51] X. Tan, G. Qin, G. Cheng, X. Song, X. Chen, W. Dai, X. Fu, Oxygen vacancies enhance photocatalytic removal of NO over an N-doped TiO₂ catalyst, *Catal. Sci. Technol.* 10 (20) (2020) 6923–6934, <https://doi.org/10.1039/d0cy01394c>.